This is an open access article published under a Creative Commons Attribution (CC-BY) License, which permits unrestricted use, distribution and reproduction in any medium, provided the author and source are cited.

ACS AUTHORCHOICE

JACS
JOURNAL OF THE AMERICAN CHEMICAL SOCIETY

pubs.acs.org/JACS

Article

Conformational and Compositional Tuning of Phenanthrocarbazole-Based Dopant-Free Hole-Transport Polymers Boosting the Performance of Perovskite Solar Cells

Zhaoyang Yao,[‡] Fuguo Zhang,[‡] Yaxiao Guo,[‡] Heng Wu, Lanlan He, Zhou Liu, Bin Cai, Yu Guo, Calvin J. Brett, Yuanyuan Li, Chinmaya Venugopal Srambickal, Xichuan Yang, Gang Chen, Jerker Widengren, Dianyi Liu, James M. Gardner, Lars Kloo, and Licheng Sun*

Cite This: *J. Am. Chem. Soc.* 2020, 142, 17681−17692

Read Online

ACCESS | Metrics & More | Article Recommendations | Supporting Information

ABSTRACT: Conjugated polymers are regarded as promising candidates for dopant-free hole-transport materials (HTMs) in efficient and stable perovskite solar cells (PSCs). Thus far, the vast majority of polymeric HTMs feature structurally complicated benzo[1,2-*b*:4,5-*b*']dithiophene (BDT) analogs and electron-withdrawing heterocycles, forming a strong donor−acceptor (D−A) structure. Herein, a new class of phenanthrocarbazole (**PC**)-based polymeric HTMs (**PC1**, **PC2**, and **PC3**) has been synthesized by inserting a **PC** unit into a polymeric thiophene or selenophene chain with the aim of enhancing the $\pi-\pi$ stacking of adjacent polymer chains and also to efficiently interact with the perovskite surface through the broad and planar conjugated backbone of the **PC**. Suitable energy levels, excellent thermostability, and humidity resistivity together with remarkable photoelectric properties are obtained via meticulously tuning the conformation and elemental composition of the polymers. As a result, PSCs containing **PC3** as dopant-free HTM show a stabilized power conversion efficiency (PCE) of 20.8% and significantly enhanced longevity, rendering one of the best types of PSCs based on dopant-free HTMs. Subsequent experimental and theoretical studies reveal that the planar conformation of the polymers contributes to an ordered and face-on stacking of the polymer chains. Furthermore, introduction of the "Lewis soft" selenium atom can passivate surface trap sites of perovskite films by Pb−Se interaction and facilitate the interfacial charge separation significantly. This work reveals the guiding principles for rational design of dopant-free polymeric HTMs and also inspires rational exploration of small molecular HTMs.

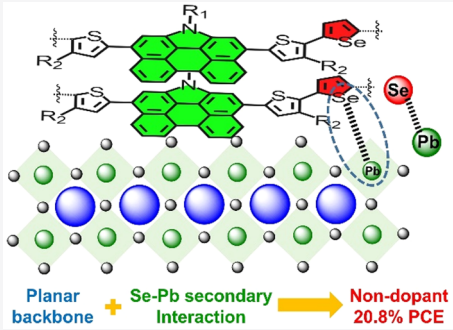

■ INTRODUCTION

Perovskite solar cells (PSCs) have gone through an unprecedented increase in power conversion efficiency (PCE) from a mere 3.8% to 25.2% in the past decade due to the excellent light-harvesting capacity and unrivalled charge-carrier diffusion length of organic−inorganic hybrid lead halide perovskites.[1−9] In spite of the rapidly surging PCE, PSCs have also caused extensive scientific studies because of their exceptional photoelectric character, facile processability, and promising commercial potential.[10−12] Recently, perovskite/Si tandem devices surpassed crystalline Si photovoltaics, displaying an exciting PCE of 29.1%, greatly boosting PSCs toward the ultimate aim of economic feasibility.[9] However, there are still several hurdles on the way to commercial application, for example, the inherent thermal and humidity instability due to the ionic nature of the perovskite crystals and the interstitial degradation caused by adverse interfacial reactions.[13−15] Therefore, massive research has focused on prolonging the lifespan of PSCs.[16−22] In particular, attenuation of PCE induced by dopants in charge-transporting layers has received special concern.[8] In a typical n-i-p device architecture, hole-transport materials (HTMs) play an imperative role in efficient hole extraction from the perovskite layer and transport to the positive electrode, preventing the moisture-sensitive perovskite material from directly touching the water molecules in ambient atmosphere. Therefore, rational selection of HTMs is very crucial for boosting the PCE and device longevity of PSCs. Thus far, a large number of organic small molecules, conjugated polymers, as well as inorganic materials have been explored as HTMs for efficient PSCs.[23−31] Among them, 2,2′,7,7′-tetrakis(*N*,*N*-di-*p*-methoxyphenylamine)-9,9′-spirobifuorene (spiro-OMeTAD)[32,33] usually serves as the state-of-the-art HTM for the benchmarking of PSCs containing new materials.[7,34] Nevertheless, despite the unique success of spiro-OMeTAD, the material still suffers from unaffordable cost and

Received: August 3, 2020
Published: September 14, 2020

© 2020 American Chemical Society

https://dx.doi.org/10.1021/jacs.0c08352
J. Am. Chem. Soc. 2020, 142, 17681−17692

tedious synthesis, probably disqualifying it from large-scale fabrication of PSCs. Even more fatal is that the steric hindrance of the spiro center gives rise to a large resistivity and low charge mobility. Therefore, introduction of proper dopants becomes necessary to increase the charge transport capacity of spiro-OMeTAD.[35−38] However, the basic problem is that the widely utilized dopants, such as lithium bis-(trifluoromethanesulfonyl)imide (LiTFSI), *tert*-butylpyridine (TBP), and cobalt metal complexes, all are hygroscopic or volatile.[39,40] Moreover, migration and relocation of the noncovalently bonded dopants usually cause morphology deterioration of the HTM layers.[41−43] All of the adverse aspects mentioned above will accelerate device deterioration significantly under a practical application environment, making the doping strategy inappropriate for production and industrialization. Therefore, a large amount of research has been devoted to exploring next-generation HTMs with the aim of improving the stability and economic feasibility of PSCs avoiding the need for dopants.[44−46] Thus far, very few of the top class PSCs containing dopant-free HTMs have been reported.

Conjugated polymers, characteristic of excellent and tunable physicochemical properties, have been widely applied in organic optoelectronic devices. Compared to some other HTMs used in PSCs, such as small molecules or inorganic materials, polymeric HTMs possess several advantages involving excellent carrier mobility, thermal and optical stability, solution processability, film-forming ability, and potential industrial production through roll-to-roll printing technologies.[47−49] Thus far, several dopant-free polymeric HTMs have been applied in PSCs and contributed to relatively high PCEs and significantly enhanced device stability.[50−57] However, nearly all known materials feature a strong donor−acceptor (D−A) structure inherited from the polymeric donors in bulk heterojunction organic solar cells (OSCs). Polymeric donors in OSCs should extract and conduct holes efficiently and at the same time act as powerful light-harvesting materials to absorb sufficient photons from sunlight.[58,59] However, HTMs in PSCs are preferably colorless and photochemically inert because the perovskite films themselves provide saturated absorption of visible light under irradiance of simulated AM 1.5G sunlight (100 mW cm^{-2}). Thus, the strong electron acceptors, which are structurally complicated and cost driving, are unnecessary in HTMs for PSCs. Bearing this in mind, we simply polymerized the widely used benzo[1,2-*b*:4,5-*b*′]-dithiophene (BDT) unit with thiophene and synthesized the low-cost **P3** (Figure S1) as a dopant-free HTM in a recent study from our lab.[60] **P3**-based PSCs provide an exceptional stabilized PCE of 20.3%, which is comparable to control devices based on doped spiro-OMeTAD. This work demonstrated that polymers without strong D−A structures could also work efficiently as HTMs in PSCs. However, the BDT analogs, which involve multiple reaction steps and dangerous reagents (*n*-BuLi, LDA, etc.) during the tedious synthesis, are still indispensable for the highly efficient HTMs in PSCs or even donor polymers in OSCs.

Perylene and its derivatives are excellent candidates for functional materials in many fields.[61,62] In this work, a series of non-BDT polymers, **PC1**, **PC2**, and **PC3**, was designed and synthesized through incorporating the large heteroatom-containing PAH unit phenanthrocarbazole (**PC**) into polymeric thiophene or selenophene chains. The obtained polymers feature suitable energy levels, excellent thermo-stability and humidity resistivity, exceptional film-forming ability, and remarkable photoelectric properties as dopant-free HTMs in PSCs. Consequently, PSCs containing **PC3** as the dopant-free HTMs showed a stabilized PCE of 20.8% and significantly enhanced stability. Experimental and theoretical studies reveal that the planar conformation of the polymers will facilitate the more ordered and face-on stacking of the polymer strands. Furthermore, introduction of the "Lewis soft" selenium element passivates the surface trap sites on the surface of perovskite films by a Pb−Se bond. The guiding principles for rational design of dopant-free polymeric HTMs are illustrated in this work.

■ RESULTS AND DISCUSSION

Figure 1 displays the molecular structures and design strategy of the three polymers **PC1**, **PC2**, and **PC3**. We first inserted

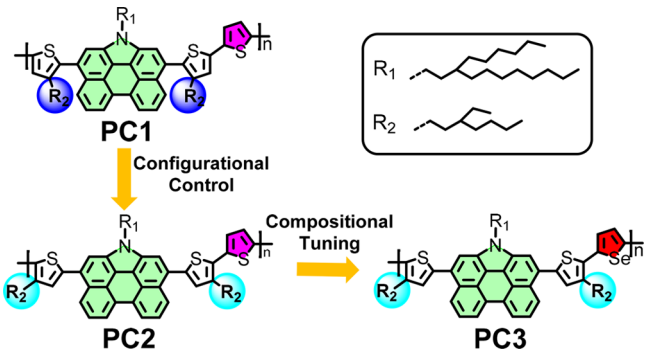

Figure 1. Molecular structures and design strategy of the three polymers **PC1**, **PC2**, and **PC3**.

PC into the polymeric thiophene chain with the aim of enhancing the $\pi-\pi$ stacking of the polymer chains and also to improve interaction with the perovskite surface through the broad and planar conjugated backbone of the **PC** unit. On the premise of strong $\pi-\pi$ stacking, several bulky and hydrophobic aliphatic chains were grafted on the rigid backbone to improve the solubility and humidity resistivity of the polymers as HTMs. From **PC1** to **PC2**, we used configurational control by changing the position of the side chains on the thiophene units. In this way, **PC2** mitigates the significant steric hindrance caused by the R_2 groups and the bulky **PC** unit, maintaining a more planar configuration. The relatively planar geometry will facilitate the $\pi-\pi$ stacking between adjacent polymer chains and most likely increase the hole mobility in the resulting HTM films. Further compositional tuning was made in **PC3** by introducing selenium, which may further improve the hole mobility through its larger polarizability. At the same time, selenium may passivate the sites of insufficiently coordinated lead ions.

Scheme 1 illustrates the synthetic routes to the three new polymers. The detailed synthetic procedures and characterization data of the new compounds are given in the Supporting Information. For the **PC1** polymer's synthesis, the reported 3,10-dibromo-1-(2-hexyldecyl)-1*H*-phenanthro[1,10,9,8-*cdefg*]carbazole (**1**)[63] was treated with *n*-butyllithium in an inert atmosphere to get a rapid halogen−lithium exchange and then transformed into its borate **2** by adding 2-isopropoxy-4,4,5,5-tetramethyl-1,3,2-dioxaborolane. The obtained **2** was cross-coupled with 2-bromo-3-(2-ethylhexyl)thiophene by a Suzuki reaction to generate the intermediate **3**, which was

https://dx.doi.org/10.1021/jacs.0c08352
J. Am. Chem. Soc. 2020, 142, 17681−17692

Scheme 1. Synthetic Routes to PC-Based Polymers[a]

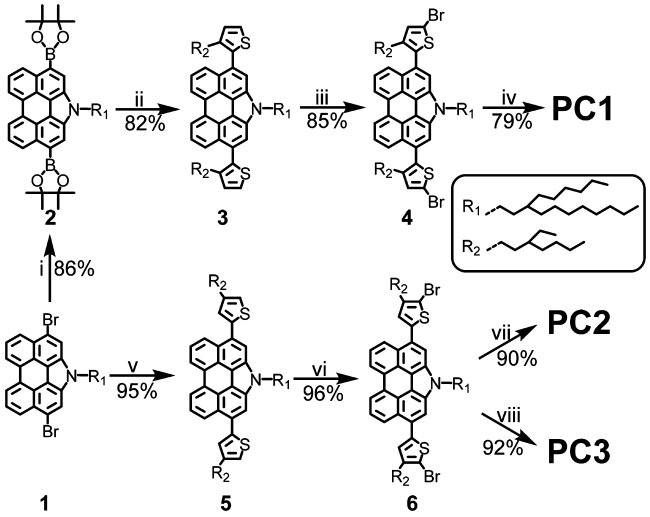

[a]Reagents and conditions: (i) *n*-BuLi, THF, −78 °C, 1 h; then 2-isopropoxy-4,4,5,5-tetramethyl-1,3,2-dioxaborolane, −78 °C to RT, 1 h; (ii) 2-bromo-3-(2-ethylhexyl)thiophene, $Pd(PPh_3)_4$, K_2CO_3, toluene/H_2O/ethanol (1/1/0.2, v/v/v), reflux, overnight; (iii) NBS, THF, 0 °C to RT, 2 h; (iv) 2,5-bis(trimethylstannyl)thiophene, $Pd_2(dba)_3$, P(*o*-tol)$_3$, chlorobenzene, reflux, 72 h; (v) (4-(2-ethylhexyl)thiophen-2-yl)trimethylstannane, $Pd_2(dba)_3$, P(*o*-tol)$_3$, toluene, reflux, 6 h; (vi) NBS, THF, 0 °C to RT, 2 h; (vii) 2,5-bis(trimethylstannyl)thiophene, $Pd_2(dba)_3$, P(*o*-tol)$_3$, chlorobenzene, reflux, 72 h; (viii) 2,5-bis(trimethylstannyl)selenophene, $Pd_2(dba)_3$, P(*o*-tol)$_3$, chlorobenzene, reflux, 72 h.

further brominated using the mild reagent NBS to give the monomer **4** in good yield. Finally, polymerization of compound **4** was achieved with 2,5-bis(trimethylstannyl)-thiophene through a Stille coupling reaction, affording the **PC1** polymer. The syntheses of **PC2** and **PC3** started with the cross-coupling reaction between compound **1** and (4-(2-ethylhexyl)thiophen-2-yl)trimethylstannane to afford **5** in an excellent yield. Thereafter, compound **5** was brominated in the presence of NBS to quantitatively yield the monomer **6**, which was further polymerized with 2,5-bis(trimethylstannyl)-thiophene and 2,5-bis(trimethylstannyl)selenophene to produce **PC2** and **PC3** in an excellent yield, respectively.

The molecular weights of the three polymers were estimated by gel permeation chromatography (GPC). The average molecular weights (M_n) were calculated as about 30, 39, and 40 kDa with polydispersity indexes (PDI) of 1.12, 1.20, and 1.19 for **PC1**, **PC2**, and **PC3**, respectively. It is well known that diverse molecular weights may give rise to differences in light absorption, hole mobility, thermal stability, and photovoltaic properties of the polymers. In order to precisely reveal the molecular structure-dependent physicochemical properties, we first investigated the repeat units of the polymers showing well-defined structures. This allows a more rational comparison between the structures and the properties. As shown in Figure 2a, the polymer segments **PC1-M**, **PC2-M**, and **PC3-M** were constructed by shortening the aliphatic chains of the polymers. The synthetic routes to **PC1-M**, **PC2-M**, and **PC3-M** and the detailed procedures are presented in Scheme S2 in the Supporting Information. Density functional theory (DFT) calculations at the level of B3LYP/6-31G(d,p) generated optimized geometries and energy levels of the frontier molecular orbitals for these three polymer fragments. A large dihedral angle of 64° between the thiophene and the **PC** unit can be observed in **PC1-M** (Figure 2b), which should be attributed to the large steric hindrance caused by the substituent groups on the thiophene unit and the bulky

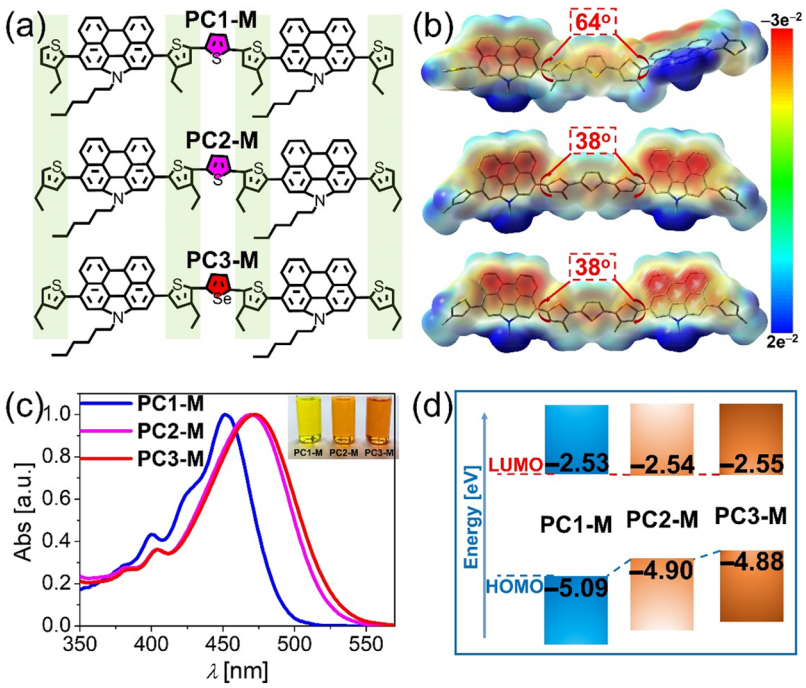

Figure 2. (a) Molecular structures of fractions (**PC1-M**, **PC2-M**, and **PC3-M**) of the **PC**-based polymers. (b) Optimized geometries and electrostatic surface potential maps (ESPs) obtained by density functional theory (DFT) calculations. Large aliphatic groups were substituted with methyl groups to accelerate the computations. Dihedral angles between the **PC** units and neighboring thiophenes are highlighted. (c) normalized electronic absorption spectra in 20 μM THF solution. (d) Energy levels derived from solution cyclic voltammetry and optical band gaps.

https://dx.doi.org/10.1021/jacs.0c08352
J. Am. Chem. Soc. 2020, 142, 17681−17692

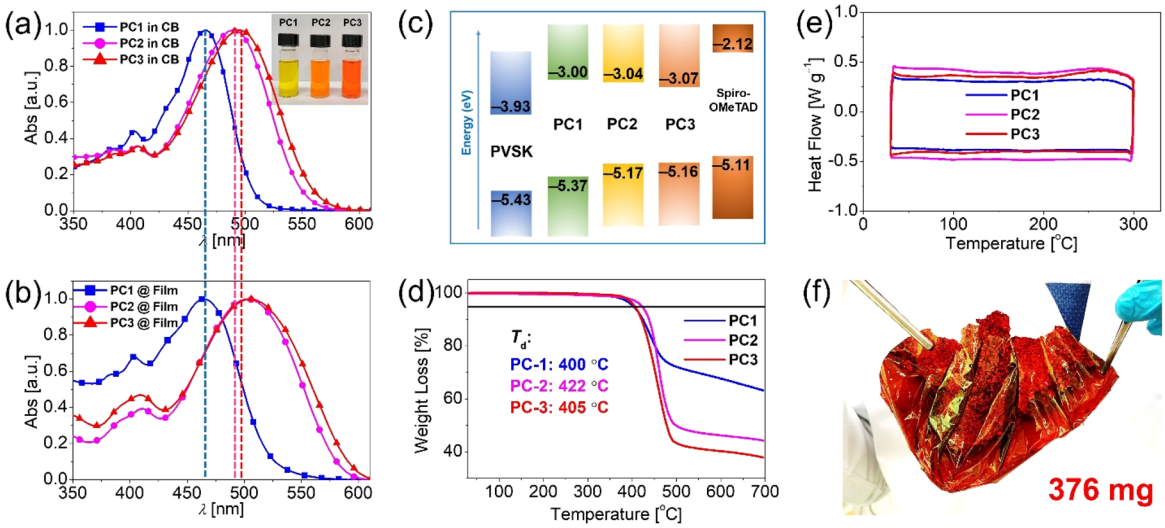

Figure 3. (a) Normalized electronic absorption spectra of the polymers **PC1**, **PC2**, and **PC3** in chlorobenzene (CB) solutions. (b) Normalized electronic absorption spectra of polymers in the solid films. (c) Energy levels of polymer films derived from CV and optical band gaps. (d) TGA traces of the polymers. (e) DSC traces of the polymers. (f) Obtained film of **PC3** polymer.

backbone of **PC**.[64] Conformational effects by changing the grafting site of the alkyl chain to the other side of the thiophene unit mitigates the steric hindrance, which contributes to a more planar backbone of **PC2-M** with respect to **PC1-M**. As might be expected, compositional tuning by introducing selenium into **PC3-M** in place of sulfur does not influence the molecular geometry significantly. The electrostatic surface potential maps (ESPs) of **PC1-M**, **PC2-M**, and **PC3-M** demonstrate the electron-rich property of the **PC** units. Consequently, the results from the theoretical calculations show relatively high energy levels of the highest occupied molecular orbitals (HOMOs) of −4.87 eV for **PC1-M**, −4.73 eV for **PC2-M**, and −4.70 eV for **PC3-M**, upshifting with the structural modifications (Figure S2). However, the lowest unoccupied molecular orbital (LUMO) energy levels are located at −2.01 eV for **PC1-M**, −2.07 eV for **PC2-M**, and −2.10 eV for **PC3-M**, giving rise to a stepwise smaller energy gap of 2.86 eV for **PC1-M**, 2.66 eV for **PC2-M**, and 2.60 eV for **PC3-M**. It is thus plausible to observe the red-shifted maximum absorption wavelength (λ_{MAX}^{Sol}) from **PC1-M** to **PC3-M** in accordance with the electronic absorption spectra of the three molecules simulated by time-dependent DFT calculations (Figure S3). The S0 → S1 vertical electronic transitions to the LUMO for three molecules occur predominantly from the HOMO, demonstrating a clear intramolecular charge-transfer character. The normalized electronic absorption spectra in THF solvent are shown in Figure 2c. λ_{MAX}^{Sol} for **PC2-M** and **PC3-M** are 469 and 473 nm, respectively, about 20 nm red shifted with respect to 451 nm for **PC1-M**. A similar trend can be also observed from the absorption spectra in the state of thin films of the molecules (Figure S4). The red-shifted absorption should be mainly attributed to the up-shifted HOMO energy levels of the constituent molecules. Cyclic voltammetry (CV) was employed to estimate the experimental energy levels of the molecules (Figure S5). The HOMO energy levels were estimated by $E = -4.8 - eE_{onset}$, where E_{onset} is the onset redox potential of a ground-state molecule in THF, being −5.09 eV for **PC1-M**, −4.90 eV for **PC2-M**, and −4.88 eV for **PC3-M** (Figure 2d). As listed in Table S1, the relative alignment of the energy levels as well as the red-shift tendency of λ_{MAX}^{Sol} are in accordance with the results from the theoretical calculations.

From molecular fragments to the polymers, we observed that all three polymers show very good solubility in several commonly used solvents, such as chloroform, toluene, and chlorobenzene, facilitating their later solution-based process for PSCs fabrication. Figure 3a and 3b shows the electronic absorption spectra of the three polymers dissolved in chlorobenzene and as solid thin films, respectively. In accordance with the absorption features noted for the **PC-M** fragment molecules, the spectra of **PC2** and **PC3** are bathochromically shifted by nearly 30 nm as compared to that of **PC1**, which can be attributed to their more planar structures. It is also notable that no obvious difference is observed regarding the maximum absorption wavelength of **PC1** from solution to a solid thin film; however, an approximate 10 nm red shift can be observed for **PC2** and **PC3**. This might imply that *J*-type aggregates, which can push the absorption toward low energies, may be formed by **PC2** and **PC3** because of their relatively planar backbones, suggesting a difference in stacking with respect to **PC1**.[65] Comparing with **PC2**, the absorption of **PC3** demonstrated a slight red shift of 3 and 6 nm in solutions and as solid films, respectively, which is expected to arise from the more electron-rich property of the Se atom than the S atom. The optical band gaps of the three polymers can be estimated as 2.37, 2.13, and 2.09 eV, respectively. Figure 3c shows the relative alignment of the energy levels of the frontier molecular orbitals as derived from the CVs of the solid thin films (Figure S6) and optical band gaps. The HOMO energy levels are determined to be −5.37 eV for **PC1**, −5.17 eV for **PC2**, and −5.16 eV for **PC3**, and the LUMO energy levels are estimated to be −3.00 eV for **PC1**, −3.04 eV for **PC2**, and −3.07 eV for **PC3**. All three polymers exhibit HOMOs and LUMOs located in a suitable energy range when comparing with the energy levels of the perovskite material used. This enables the polymers to efficiently extract holes from the perovskite film and simultaneously block the reverse electron flow from the perovskite to the metal back contact. Furthermore, we

https://dx.doi.org/10.1021/jacs.0c08352
J. Am. Chem. Soc. 2020, 142, 17681−17692

performed thermal gravimetric analysis (TGA) and differential scanning calorimetry (DSC) to monitor the phase stability of the polymers under thermal stress. As revealed in Figure 3d and 3e, the decomposition temperatures, defined as having lost 5% weight, are 400, 422, and 405 °C for **PC1**, **PC2**, and **PC3**, respectively. No obvious peaks can be noticed in the DSC curves at lower temperatures, suggesting that the polymers are thermally stable without detectable phase transitions up to 300 °C. All of the polymers thus display low crystallinity and high thermal stability in the film state, which is a prerequisite for durable device operation. The **PC3** polymer forms an exceptionally compact film, which can be attributed to the strong $\pi-\pi$ stacking of the broad and planar conjugated backbone of **PC** (Figure 3f). The excellent film-forming ability of the polymers can facilitate effective coverage of the perovskite surface even at a low amount of material. The detailed parameters of the optical, thermal, and electrochemical properties are listed in Table S2.

An adequate charge-transporting ability is vital for the polymeric materials to become useful as HTMs in PSCs, and therefore, hole-only devices with the structure of ITO/poly(3,4-ethylenedioxythiophene)-poly(styrenesulfonate) (PEDOT:PSS)/HTM/Au were constructed to measure the hole mobility of the HTMs by utilizing the space charge-limited current (SCLC) method. As displayed in Figure 4a, the estimated hole mobilities (μ_h) of **PC2** and **PC3** are 7.3×10^{-4} and 8.1×10^{-4} cm^2 V^{-1} s^{-1}, respectively, demonstrating over 1 order of magnitude higher mobility than that of **PC1**, being 4.2×10^{-5} cm^2 V^{-1} s^{-1}. The slightly higher μ_h of **PC3** with respect to **PC2** can be probably rationalized as an effect of the incorporated selenium atom in the structures given the only structural change is the replacement of sulfur with selenium. However, the dramatic differences of μ_h between the two "isomers" **PC1** and **PC2** are expected to be correlated to the significantly different geometries of the respective polymeric backbones (twisted for **PC1** and planar for **PC2**).

In order to gain insight into the underlying correlation between μ_h and the molecular packing, grazing-incidence wide-angle X-ray scattering (GIWAXS) experiments were carried out (Figure S7).[66,67] As observed from Figure 4b and 4c, **PC2** and **PC3** mainly feature a typical face-on orientation as discerned from the apparent peaks in the in-plane direction ($q_r \approx 0.29$ Å^{-1}) and the out-of-plane direction ($q_z \approx 1.5$ Å^{-1}). In contrast, the **PC1** polymer displays a much weaker peak at $q_z \approx 1.4$ Å^{-1} along the out-of-plane direction and an unambiguous lattice plane (100) in the in-plane direction, suggesting a more edge-on orientation of molecular stacking. The edge-on orientation is expected to impede efficient charge transport in the vertical diode architecture of solar cells.[68] These results are in accordance with the lower hole mobility observed for **PC1** film as compared to that of **PC2** and **PC3**. Furthermore, **PC2** and **PC3** display a shorter $\pi-\pi$ stacking distance of ~4.1 Å with respect to that of 4.5 Å for **PC1**, further confirming that the planar polymer backbone favors a more compact packing of the polymer chains through secondary interactions. The closer stacking may enhance an effective overlap of orbitals between the neighboring polymer strands, facilitating charge mobility.[69] Meanwhile, the optimized stacking models by piling up three layers of polymers were obtained by the DFT calculations (Figure 4d). As might be expected, **PC2** and **PC3** exhibit a more ordered molecular packing pattern than **PC1** due to their more planar conformations. This is in good agreement with the results from the experiments. To

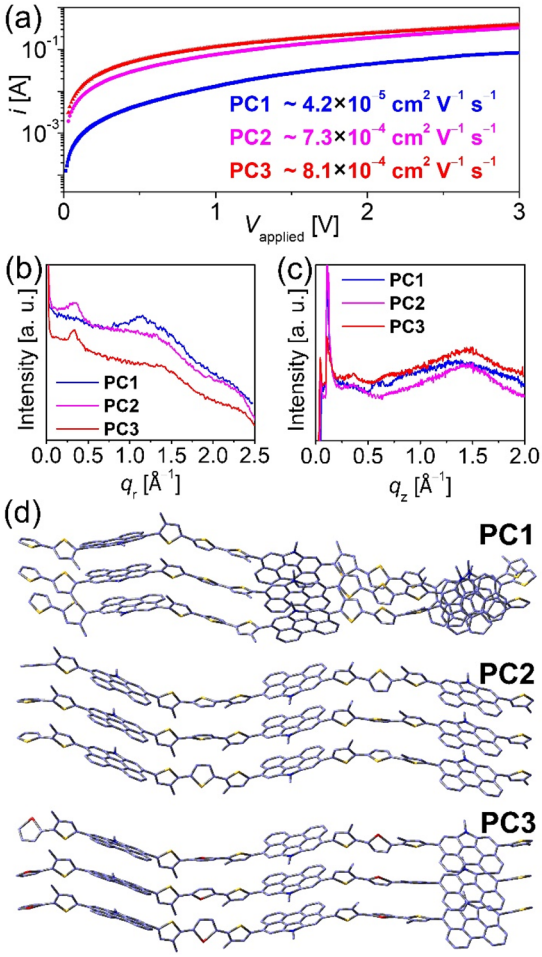

Figure 4. (a) Hole mobilities of the three polymers derived from SCLC measurements. (b) In-plane and (c) out-of-plane line cuts of the 2D GIWAXS traces for the three polymers on silicon substrates. (d) Optimized stacking models obtained by DFT calculations.

summarize, all of the above experimental and theoretical modeling results are in good agreement with the lower vertical μ_h of **PC1** as compared to **PC2** and **PC3**. Moreover, molecular stacking effects on the absorption differences of the three polymers going from solutions to thin solid films emerge as a logical consequence. The face-on orientation as well as the sequentially compact polymer stacking in **PC2** and **PC3** are expected to result in better performance of the resulting PSC devices as compared to those based on **PC1**. In order to investigate the film morphology of the polymers when coated on top of the perovskite films, field emission scanning electron microscopy (FE-SEM) and atomic force microscopy (AFM) were performed. Figure S8 displays the SEM images of the noncovered perovskite surface and with the three polymers capping perovskite films. The excellent film-processing ability attributed to the planar backbones in **PC2** and **PC3** results in uniform films that clad the surface of the perovskite layers perfectly. AFM images were further analyzed to extract morphology information on the perovskite films covered by the different polymers on a nanoscale level. As displayed in Figure S9, the root-mean-square (RMS) roughness amounts of **PC1**, **PC2**, and **PC3** were estimated to be 13, 12, and 11 nm, respectively, significantly smaller than that of neat perovskite film (20 nm; the estimated statistical error of the roughness is less than 0.5 nm). The complete and uniform coverage by the

https://dx.doi.org/10.1021/jacs.0c08352
J. Am. Chem. Soc. 2020, 142, 17681−17692

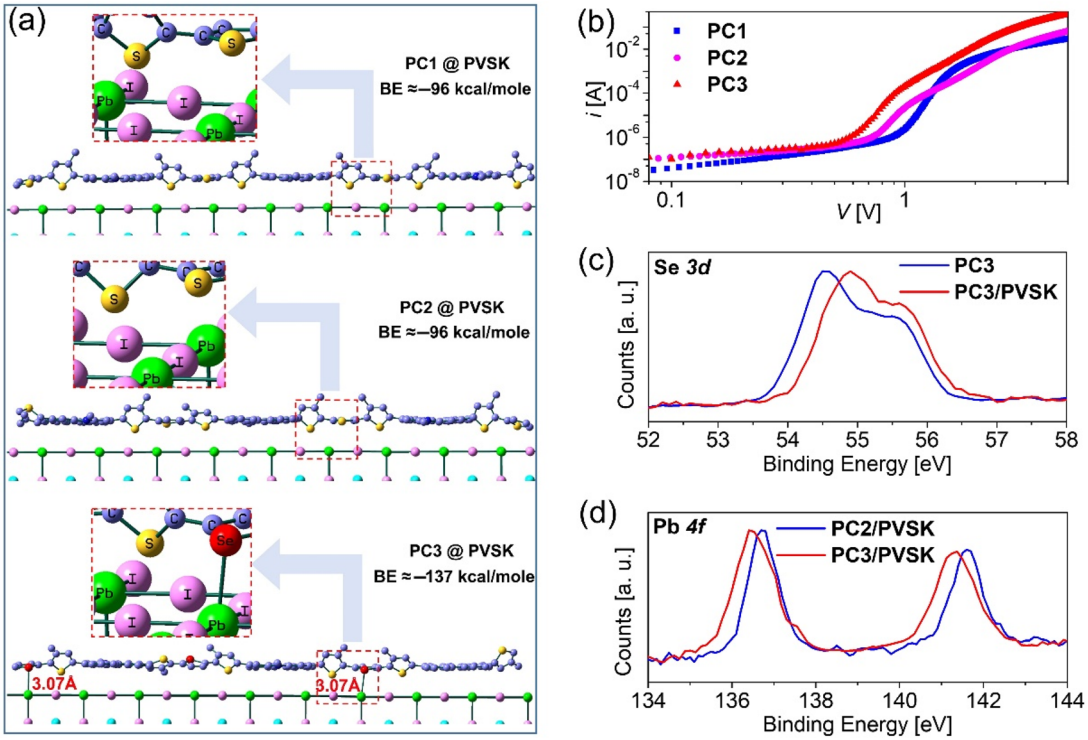

Figure 5. (a) Theoretically modeled stacking patterns of the **PC** polymers on top of a perovskite (PVSK) surface. Binding energies (BE) between the polymers and the perovskite surface are given. (b) Trap state densities of the **PC** polymers coating perovskite films. (c) XPS signals of Se 3d from a pristine **PC3** film and from a **PC3**-coated perovskite film. (d) XPS signals of Pb 4f from **PC2**- and **PC3**-coated perovskite films.

polymers prevents the perovskite layer from direct contact with the counter electrode materials and may thus significantly reduce undesired shunt losses in the resulting PSCs.

Considerations concerning the perovskite surface passivation by electron-rich heteroatoms were behind our rational inclusion of abundant nitrogen, sulfur, and selenium elements into the new **PC**-based polymeric HTMs. Thus far, the widely utilized passivators have been confined to the oxygen-, nitrogen-, and sulfur-containing compounds.[7,70] However, selenium-involved passivators are rarely reported in the literature. The empirical covalent radius and calculated atomic radius of selenium are 115 and 103 pm, respectively, clearly larger than those of 100 and 88 pm for sulfur.[71,72] Therefore, the larger atomic radius and "Lewis softer" selenium atom represents a characteristic example of a highly electron-rich, easy polarizable, and relatively large element. Therefore, selenium has properties that may offer efficient surface passivation to stabilize coordinatively unsaturated lead ion at the perovskite−HTM interface. In order to investigate the secondary interaction between polymeric HTMs and the perovskite films, DFT calculations were conducted by positioning three repeat segments of polymeric HTMs on the top of a perovskite crystal model with subsequent constraint optimization. As demonstrated in Figure 5a and Figure S10, all three polymeric HTMs interact tightly with the perovskite surface through the rigid and bulk conjugated plane of **PC**. This gives support to the strategy of our design of introducing large PAH units to enhance the interfacial packing between the perovskite surface and the HTMs. It is worth noting that the selenium atoms in **PC3** are prone to approach lead sites at the perovskite surface, forming weak but specific interactions characterized by a bond length of 3.07 Å, resulting in a binding energy of −137 kcal/mol between the **PC3** segment and perovskite layer, which is much larger than that of −96 kcal/mol obtained for the **PC1** and **PC2** systems. The tighter packing will lead to a larger orbital overlap at the perovskite/HTM interface and consequently facilitate hole extraction. The trap state sites on the surface of the perovskite film can be partially passivated by Lewis bases, such as the electron-rich atoms being part of the HTMs as discussed above, indicating the extent of passivation by the HTMs. Thereby, we made specific devices with an architecture of ITO/PEDOT:PSS/$MAPbI_3$/HTM/Au to estimate the trap-state densities directly and further evaluate the passivation effects of the three HTMs (Figure 5b). The trap-filling-limited voltages (V_{TFL}) of the three dopant-free **PC1**-, **PC2**-, and **PC3**-coated perovskite films were obtained as 0.91, 0.72, and 0.54 V, respectively. The corresponding trap-state densities were determined to 1.55×10^{16}, 1.21×10^{16}, and 9.2×10^{15} cm^{-3}, respectively. The significantly lower trap-state density of the perovskite surfaces capped by **PC3** should be attributed to the higher passivation effect of selenium. This is in good agreement with the results from our DFT modeling. The lower density of trap states for **PC3**-coated perovskite films will be expected to generate fewer recombination centers and thus afford a better photovoltaic performance. X-ray photoelectron spectroscopy (XPS) was carried out to monitor the energy change of characteristic peaks caused by selenium passivation (Figure 5c and 5d). The Se 3d peak of **PC3**-coated perovskite films is located at 54.9 eV, shifting to a higher binding energy with respect to the 54.6 eV for a pristine **PC3** film. This indicates a direct interaction between selenium in **PC3** and the perovskite surface. The symmetric peaks that appear at 136.7 and 141.6 eV of **PC2**-capped perovskite films should be ascribed to the Pb 4f core level. The spin−orbit split of 4.8 eV between the 4f $_{7/2}$ and the 4f $_{5/2}$ peaks is in good accordance

https://dx.doi.org/10.1021/jacs.0c08352
J. Am. Chem. Soc. 2020, 142, 17681−17692

with reported values.[73] However, for the **PC3**-capped perovskite films, these peaks appear at 136.4 and 141.3 eV, showing a ~0.3 eV shift toward the low-binding energy direction. These shifts should be attributed to the Pb−Se interaction mediated by the **PC3** polymer and perovskite surface.

Steady-state PL spectra (Figure 6a) and time-resolved PL decay (TRPL) traces (Figure 6b) were recorded to elucidate

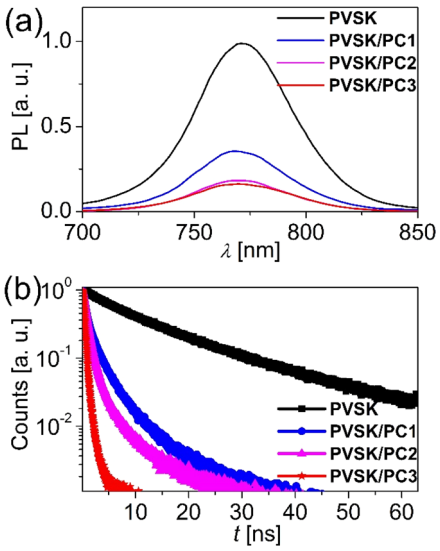

Figure 6. (a) Steady-state photoluminescence (PL) spectra and (b) time-resolved PL decay traces of the perovskite films (PVSK) and HTM-capped perovskite films.

the interfacial charge transfer between the three polymers and the perovskite films. Capping with diverse HTMs will evoke PL quenching of the perovskite films, indicating hole extraction at the energy-offset HTM/perovskite interface. With respect to **PC1**-capped perovskite film, **PC2**- and **PC3**-capped ones display a clearly more efficient depression of the perovskite PL intensity. This may be partly caused by the larger hole mobility and upshifted HOMO energy levels of these polymers which will provide a larger driving force for hole collection. The TRPL decay traces can be modeled by a biexponential equation, and the obtained parameters are given in Table S3. The results are in good agreement with the steady-state PL spectra, where a dramatically reduced PL lifetime can be observed when the pure perovskite film is capped by the polymers. Among the polymers, the **PC3** system demonstrates a reduced PL lifetime with respect to the other two polymers, suggesting a more efficient hole extraction from the perovskite film to the HTM layer.

In order to explore application of the polymers as dopant-free HTMs, PSCs with the regular architecture of glass/FTO (flourine-doped tin oxide)/mesoporous SnO_2/perovskite/HTM/Au were assembled (Figure 7a).[74] All of the polymers were applied as HTMs without any dopants in this work. The detailed fabrication of PSCs is described in the Supporting Information. We first investigated the device performance related to the HTM film thickness by adjusting the concentrations of the HTM precursors from 3 to 10 mg/mL in chlorobenzene, and the obtained photovoltaic parameters are displayed in the Supporting Information (Figure S11 and Table S4). All three polymers showed the best device performance at a low precursor concentration, about 5 mg/mL, which is markedly less than the >80 mg/mL necessary for

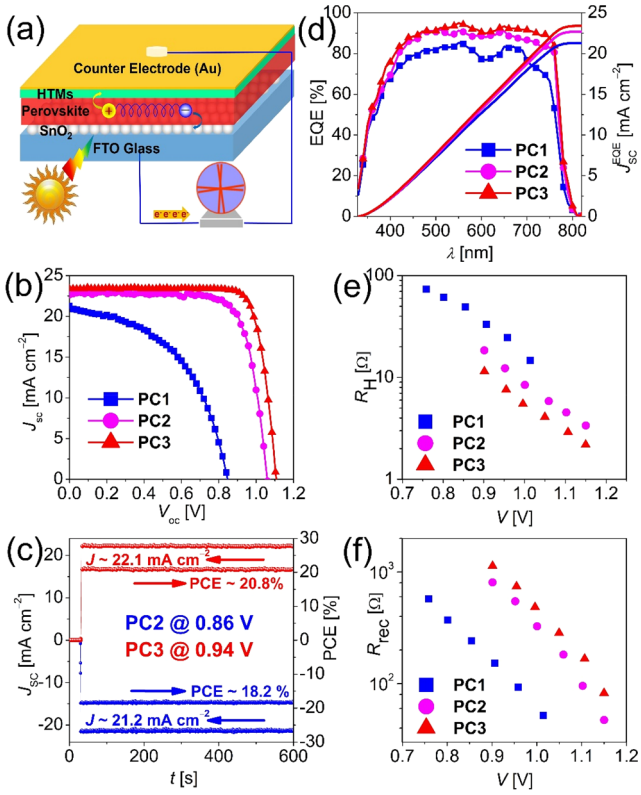

Figure 7. (a) Schematic structure of the PSCs studied. (b) External quantum efficiencies (EQEs) and the corresponding J_{SC}^{EQE} derived from the **PC1**-, **PC2**-, and **PC3**-based PSC devices. (c) J−V curves obtained under irradiance of 100 mW cm^{-2}. (d) Steady-state output of photocurrent density and PCE recorded at the maximum power point (MPP) under AM 1.5G illumination. (e) Potential bias-dependent hole transport resistance (R_H) of the PSCs. (f) Potential bias-dependent interface recombination resistance (R_{REC}) of the PSCs.

spiro-OMeTAD. The perfect coverage of the perovskite surface at the low concentration of the HTMs can be ascribed to the excellent film-forming ability of **PC** polymers, which in turn can be attributed to the planar backbone-induced strong interchain coupling (π−π stacking) between adjacent polymer strands. The resistance and electrochemical impedance spectra of **PC3** films of different thicknesses (Figure S11b and S11c) demonstrate that the higher resistance of the thicker films (10 mg/mL precursor solution concentration) is almost twice as high as that for the thinner films (5 mg/mL), which most likely will be responsible for the lower FF exhibited by the PSCs based on the thicker films. The low polymer amounts necessary will result in low-cost PSCs when taking the scaling of HTMs into consideration (Figures S12−S16, Tables S5−S7). Several key intermediates during the synthesis of **PC3** are not commercially available at this moment, which will inevitably push the human resource and materials costs up. However, the significant cost advantage for per cell (low concentration, dopant free, etc.) with respect to that of spiro-OMeTAD still qualifies **PC3** as a promising candidate for large-scale production of PSCs. Figure 7b shows the optimized J−V curves by reverse scanning, and detailed photovoltaic parameters are collected in Table 1. PSCs based on the **PC1** HTM display an inferior PCE of 8.8% with a relatively good short-circuit current density, J_{SC}, of 21.3 mA·cm^{-2}. However, the PSCs also show a low open-circuit voltage, V_{OC}, of 0.85 V

https://dx.doi.org/10.1021/jacs.0c08352
J. Am. Chem. Soc. 2020, 142, 17681−17692

Table 1. Photovoltaic Parameters of Champion PSCs Based on Dopant-Free Polymeric HTMs and Doped Spiro-OMeTAD[a]

HTMs	J_{SC}^{EQE} [mA cm^{-2}]	J_{SC} [mA cm^{-2}]	V_{OC} [V]	FF [%]	PCE [%]
PC1	21.1	21.3	0.85	49.1	8.8
PC2	22.6	22.7	1.06	76.2	18.3
PC3	23.5	23.5	1.11	80.0	20.8
Spiro-OMeTAD	23.2	23.3	1.10	78.8	20.3 (doped)

[a] J_{SC}^{EQE} was calculated via wavelength integration of the standard AM1.5G emission spectrum.

and fill factor, FF, of 49.1% along with a problematic hysteresis effect (Figure S17). Obviously, the low hole mobility of **PC1** manifests itself in the inefficient PSCs. In contrast, after configurational tuning of the polymer backbone structure, **PC2**-based PSCs demonstrate much better performance with a good PCE of 18.3% together with a J_{SC} of 22.7 mA·cm^{-2}, a V_{OC} of 1.06 V, and a FF of 76.2%. Meanwhile, no obvious hysteresis effect can be observed for **PC2**-based PSCs. As shown above, inclusion of Se increased the hole mobility of **PC3** as well as improved the passivation of the perovskite surface. As a result, a better PCE of 20.8% was displayed by **PC3**-based PSCs with negligible hysteresis, generating an excellent J_{SC} of 23.5 mA·cm^{-2}, V_{OC} of 1.11 V, and FF of 80.0%, ranking this type of PSC as one of the best reported by employing dopant-free HTMs. The **PC3**-based PSCs are superior to the reference one including doped spiro-OMeTAD as HTM (Figure S18). Furthermore, the power output at the maximum power point (MPP) was recorded for 1500 s, and highly stable PCEs of 18.2% and 20.8% are obtained for **PC2**- and **PC3**-based PSCs, respectively (Figure 7c). It is notable that all of the photovoltaic results are in good agreement with the structure-based analysis and prediction above. As shown in Figure 7d, external quantum efficiencies (EQEs) were obtained for the PSCs based on the three dopant-free HTMs as a function of wavelength. **PC2**- and **PC3**-based PSCs both show excellent EQEs in a broad range from 400 to 800 nm, generating integrated J_{SC}^{EQE} of 22.6 and 23.5 mA·cm^{-2}, respectively. Nevertheless, The J_{SC}^{EQE} of 21.1 mA·cm^{-2} for **PC1**-based PSCs is much lower than those of **PC2**- and **PC3**-based devices, which should be ascribed to its poor charge extraction properties. All of the J_{SC}^{EQE} calculated from the EQEs are in good accordance with the J_{SC} depicted in Figure 7b.

From the cross-sectional SEM image of **PC3**-based PSCs, a ca. 40 nm thick HTM layer can be observed, showing the uniform and complete coverage of the surface of the ∼450 nm thick perovskite layer (Figure S19). For **PC1**, the performance of the resulting PSCs is significantly lower as the concentration of HTM precursors is increased from 5 to 10 mg/mL, especially regarding the FF and V_{OC}. Most likely a thicker film suffers from the charge transport losses due to the intrinsically low conductivity of the organic materials. However, **PC3**-based PSCs exhibit comparable PCEs independent of the precursor concentration changes, which should be attributed to the high hole mobility of **PC3**. The PCEs independent of the HTM thickness are crucial for the conformity rate in future scalable roll-to-roll printing production. A lower concentration of HTM precursors than 5 mg/mL will give rise to incomplete coverage of the perovskite surface, resulting in severe shunt loss at the interface. We carried out a statistical analysis of 30 devices for PSCs based on each polymer to monitor the reproducibility of **PC1**-, **PC2**-, and **PC3**-based PSCs. As displayed in Figure S20, the distribution of the median PCE gets more narrow going from **PC1**- to **PC3**-based PSCs, probably reflecting a hole mobility dependency. In order to track the synthetic reproducibility of **PC3**, three different batches were synthesized and applied in PSCs. As shown in Figure S21, the statistic PCEs of PSCs suggest excellent synthetic reproducibility and device reproducibility of **PC3**, extricating **PC3**-based PSCs from vulnerable device fabrication, especially for large-scale production. In order to gain insights into the origin of V_{OC} and FF variations, we employed electrochemical impedance spectroscopy (EIS) at a range of potential bias. A simplified equivalent circuit model used for analysis is presented in the Supporting Information. The model unveiled two key parameters, R_H and R_{rec},[75] where R_H represents the transport resistance of the hole-transport layer and R_{rec} is determined by the charge recombination resistance at the HTM/perovskite interface. As shown in Figure 7e, the PSCs of **PC1**, **PC2**, and **PC3** exhibit a stepwise lower R_H at a given potential bias, which can be ascribed to the stepwise increase of thin film hole mobility. At the same potential bias, an incremental R_{rec} going from **PC1** to **PC3** can be observed (Figure 7f), indicating a retarded interfacial charge recombination for **PC3**-based PSCs. Overall, the higher R_{rec} and lower R_H agree well with the observed higher V_{OC} and higher FF for **PC3**-based PSCs. The V_{OC} trend of **PC1** > **PC2** > **PC3** will be affected by a multitude of effects, such as the quality of coverage of the perovskite film by the polymers and the density of trap states on the surface of the perovskite film. The low V_{OC} of **PC1**-based devices is mainly caused by the poor coverage of the perovskite film by **PC1** (Figure S8). The higher V_{OC} of **PC3**-based devices, with respect to that of **PC2**, can be attributed to the strong passivation effects of selenium reducing the density of the trap state sites on the surface of the perovskite film. Therefore, it is reasonable that the lower densities of the trap states (Figure 5b) cause the interface recombination resistances to become higher (Figure 7f) going from **PC1** to **PC3**.

Moisture-induced decomposition of the perovskite film is a critical degradation path for PSCs. Consequently, in our rational design of the **PC**-based polymeric HTMs, a number of bulky and hydrophobic aliphatic chains were introduced to improve the water-repelling properties of the resulting HTM-coated perovskite films. In general, the alkyl groups usually disturb the interaction between the HTMs and the perovskite films and thus hinder efficient charge transfer. However, in the current systems, a delicate balance was established to maintain excellent humidity resistivity on the premise of a highly strong interface interaction by introducing the **PC** units as well as selenium in the polymer candidates. Quite large contact angles (∼100°) with respect to water droplets were obtained by the **PC**-based polymers when applied as capping layers with respect to the neat perovskite film (∼60°). This indicates an excellent protection of the hygroscopic perovskite material from moisture by the **PC**-based polymers (Figure S22). The device stability of our champion PSCs containing **PC3** as the dopant-free HTM was investigated and compared to a device based on the well-known spiro-OMeTAD (Figure S23). The devices were first placed under ambient atmosphere with

https://dx.doi.org/10.1021/jacs.0c08352
J. Am. Chem. Soc. 2020, 142, 17681−17692

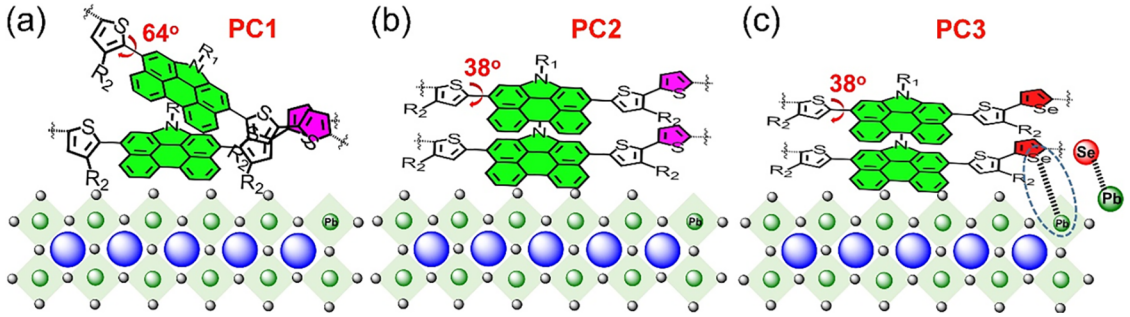

Figure 8. Schematic stacking models of the polymers including the perovskite surface: (a) **PC1**, (b) **PC2**, and (c) **PC3**.

indoor light. The PSCs capped with **PC3** as dopant-free HTM layer maintained a nearly unaltered PCE after 1000 h with respect to the original one. In contrast, the control PSCs coated by doped spiro-OMeTAD suffered a dramatic decrease of PCE during the test. Subsequently, the stability of the PSCs was further evaluated under continuous AM1.5 G equivalent light irradiation at 40 and 85 °C. After a fast initial burn-in decay, likely involving migration of the A-site cations in the perovskite,[29] the **PC3**-based PSCs remained highly stable at 40 °C. However, the control PSCs based on doped spiro-OMeTAD display a >80% PCE loss after 1000 h. This should be attributed to the hygroscopic dopants FK209, TBP, and LiTFSI used in combination with spiro-OMeTAD, which will definitely accelerate the decomposition of perovskite films involving water. The obvious PCE decrease of PSCs at 85 °C should be attributed to the insufficient thermal stability of perovskite materials. The stability test highlights the remarkable ability of the dopant-free polymers studied in this work to generate excellent photovoltaic performance and excellent durability of the resulting PSC devices.

Figure 8 displays schematic stacking models of **PC**-based polymers and the interaction with a perovskite surface, giving us an image for rational design of dopant-free polymeric HTMs. Despite well-known prerequisites, (1) a well-aligned HOMO energy level with respect to the perovskite valence band (VB) to extract holes in near unity yield, (2) significantly higher LUMO energy level than the perovskite conduction band bottom (CB) to obstruct contrary electron flow, (3) good hole mobility for efficient charge extraction and transport, and (4) excellent thermal and optical phase stability, several guiding design principles directly correlated to the molecular structure have also been highlighted in this work. First, a large conjugated system with a rigid and planar backbone can be inserted into the polymer chains to enhance the $\pi-\pi$ stacking of adjacent polymer strands and also with the perovskite surface. Second, the suitable dihedral angles should be addressed between the broad backbone and connected units. A too large dihedral angle may result in disordered packing of the polymers strands. This may, from a design point of view, be a difficult balance since a too small dihedral angle may induce low solubility and therefore become an obstacle for solution processing. Third, several bulky and hydrophobic alkyl chains can be grafted on the polymeric backbone to improve the humidity resistivity and solubility of polymer provided that strong $\pi-\pi$ stacking is not prevented. Finally, several "Lewis soft" atoms, characteristic of being highly electron-rich and having a large atomic radius, can be introduced as efficient passivators to bond to coordinatively unsaturated lead ions at the surface of the perovskite layer and to enhance the interfacial charge transfer.

■ CONCLUSION

To summarize, we synthesized a series of novel and cost-effective polymeric semiconductors **PC1**, **PC2**, and **PC3** characterized by a rigid **PC** plane and explored their application as dopant-free HTMs in PSCs. Introduction of a broad and planar **PC** unit significantly enhanced the $\pi-\pi$ stacking of adjacent polymer strands as well as the interaction with the perovskite surface. The configurational control of **PC1** mitigates the huge steric hindrance between combined units and generates a more planar geometry as realized in **PC2**, promoting a face-on-oriented stacking and good charge transport properties. Subsequently, compositional tuning by introducing the "Lewis soft" selenium element improved passivation of the trap-state defects at the **PC** polymer/perovskite interface and thereby reduced recombination losses. As a consequence, the PSCs based on the well-designed **PC3** gave rise to an excellent PCE of 20.8%, ranking as one of the best performances recorded by PSCs based on dopant-free HTMs. Benefiting from the very strong polymer strand stacking promoted by the **PC** units, several bulky and hydrophobic aliphatic chains can be grafted on the polymer backbone without restraining interstrand orbital overlap and thereby hole mobility. The excellent humidity resistivity of the polymers resulted in excellent PSC device durability and morphology stability under the dual pressure of thermal stress and light soaking. The combination of excellent PCE and long-term stability for PSCs based on the newly designed **PC3** polymer offer an encouraging platform for commercially feasible PSCs. Several guiding principles for further rational design of dopant-free polymeric HTMs are also revealed in this work.

■ ASSOCIATED CONTENT

Supporting Information

The Supporting Information is available free of charge at https://pubs.acs.org/doi/10.1021/jacs.0c08352.

Detailed description of the experimental methods, including molecular synthesis, film deposition, device fabrication and characterization, additional data and figures, and NMR spectra (PDF)

■ AUTHOR INFORMATION

Corresponding Author

Licheng Sun − *Department of Chemistry, Organic Chemistry, KTH Royal Institute of Technology, Stockholm 10044, Sweden; State Key Laboratory of Fine Chemicals, Institute of Artificial*

https://dx.doi.org/10.1021/jacs.0c08352
J. Am. Chem. Soc. 2020, 142, 17681−17692

Photosynthesis, DUT−KTH Joint Education and Research Centre on Molecular Devices, Dalian University of Technology (DUT), Dalian 116024, China; Center of Artificial Photosynthesis for Solar Fuels, School of Science, Westlake University, Hangzhou 310024, China; orcid.org/0000-0002-4521-2870; Email: lichengs@kth.se

Authors

Zhaoyang Yao − *Department of Chemistry, Organic Chemistry, KTH Royal Institute of Technology, Stockholm 10044, Sweden*

Fuguo Zhang − *Department of Chemistry, Organic Chemistry, KTH Royal Institute of Technology, Stockholm 10044, Sweden;* orcid.org/0000-0002-2789-7714

Yaxiao Guo − *Department of Chemistry, Organic Chemistry, KTH Royal Institute of Technology, Stockholm 10044, Sweden*

Heng Wu − *Department of Chemistry, Zhejiang University, Hangzhou 310028, China*

Lanlan He − *Department of Chemistry, Applied Physical Chemistry, KTH Royal Institute of Technology, Stockholm 10044, Sweden*

Zhou Liu − *School of Physical Science and Technology, ShanghaiTech University, Shanghai 201210, China*

Bin Cai − *State Key Laboratory of Fine Chemicals, Institute of Artificial Photosynthesis, DUT−KTH Joint Education and Research Centre on Molecular Devices, Dalian University of Technology (DUT), Dalian 116024, China*

Yu Guo − *Department of Chemistry, Applied Physical Chemistry, KTH Royal Institute of Technology, Stockholm 10044, Sweden*

Calvin J. Brett − *Deutsches Elektronen-Synchrotron (DESY), Hamburg 22607, Germany; Department of Engineering Mechanics and Wallenberg Wood Science Center, KTH Royal Institute of Technology, Stockholm 10044, Sweden;* orcid.org/0000-0001-5789-6299

Yuanyuan Li − *Wallenberg Wood Science Center, Department of Fibre and Polymer Technology, KTH Royal Institute of Technology, Stockholm 10044, Sweden;* orcid.org/0000-0002-1591-5815

Chinmaya Venugopal Srambickal − *Experimental Biomolecular Physics, Department of Applied Physics, KTH Royal Institute of Technology, Stockholm SE-10691, Sweden*

Xichuan Yang − *State Key Laboratory of Fine Chemicals, Institute of Artificial Photosynthesis, DUT−KTH Joint Education and Research Centre on Molecular Devices, Dalian University of Technology (DUT), Dalian 116024, China;* orcid.org/0000-0002-3035-4163

Gang Chen − *School of Physical Science and Technology, ShanghaiTech University, Shanghai 201210, China;* orcid.org/0000-0001-8112-3579

Jerker Widengren − *Experimental Biomolecular Physics, Department of Applied Physics, KTH Royal Institute of Technology, Stockholm SE-10691, Sweden;* orcid.org/0000-0003-3200-0374

Dianyi Liu − *School of Engineering, Westlake University, Hangzhou 310024, China*

James M. Gardner − *Department of Chemistry, Applied Physical Chemistry, KTH Royal Institute of Technology, Stockholm 10044, Sweden;* orcid.org/0000-0002-4782-4969

Lars Kloo − *Department of Chemistry, Applied Physical Chemistry, KTH Royal Institute of Technology, Stockholm 10044, Sweden;* orcid.org/0000-0002-0168-2942

Complete contact information is available at: https://pubs.acs.org/10.1021/jacs.0c08352

Author Contributions

‡Z.Y., F. Z., and Y.G.: These authors contributed equally.

Notes

The authors declare no competing financial interest.

■ ACKNOWLEDGMENTS

This work was financially supported by the Swedish Energy Agency, the Swedish Research Council, the Knut and Alice Wallenberg Foundation, the Swedish government by STandUP for ENERGY and the Swedish Strategic Research Foundation-SSF (RAM15-0130), and the National Natural Science Foundation of China (21120102036 and 91233201). We thank the National Supercomputer Centre at Linköping University for computation resources.

■ REFERENCES

(1) Kojima, A.; Teshima, K.; Shirai, Y.; Miyasaka, T. Organometal Halide Perovskites as Visible-Light Sensitizers for Photovoltaic Cells. *J. Am. Chem. Soc.* **2009**, *131* (17), 6050−6051.

(2) Kim, H.-S.; Lee, C.-R.; Im, J.-H.; Lee, K.-B.; Moehl, T.; Marchioro, A.; Moon, S.-J.; Humphry-Baker, R.; Yum, J.-H.; Moser, J. E.; Grätzel, M.; Park, N.-G. Lead Iodide Perovskite Sensitized All-Solid-State Submicron Thin Film Mesoscopic Solar Cell with Efficiency Exceeding 9%. *Sci. Rep.* **2012**, *2* (1), 591.

(3) Lee, M. M.; Teuscher, J.; Miyasaka, T.; Murakami, T. N.; Snaith, H. J. Efficient Hybrid Solar Cells Based on Meso-Superstructured Organometal Halide Perovskites. *Science* **2012**, *338* (6107), 643−647.

(4) Yang, W. S.; Park, B.-W.; Jung, E. H.; Jeon, N. J.; Kim, Y. C.; Lee, D. U.; Shin, S. S.; Seo, J.; Kim, E. K.; Noh, J. H.; Seok, S. I. Iodide Management in Formamidinium-Lead-Halide−Based Perovskite Layers for Efficient Solar Cells. *Science* **2017**, *356* (6345), 1376−1379.

(5) Jeon, N. J.; Na, H.; Jung, E. H.; Yang, T.-Y.; Lee, Y. G.; Kim, G.; Shin, H.-W.; Il Seok, S.; Lee, J.; Seo, J. A Fluorene-Terminated Hole-Transporting Material for Highly Efficient and Stable Perovskite Solar Cells. *Nat. Energy* **2018**, *3* (8), 682−689.

(6) Jung, E. H.; Jeon, N. J.; Park, E. Y.; Moon, C. S.; Shin, T. J.; Yang, T.-Y.; Noh, J. H.; Seo, J. Efficient, Stable and Scalable Perovskite Solar Cells Using Poly(3-hexylthiophene). *Nature* **2019**, *567* (7749), 511−515.

(7) Jiang, Q.; Zhao, Y.; Zhang, X.; Yang, X.; Chen, Y.; Chu, Z.; Ye, Q.; Li, X.; Yin, Z.; You, J. Surface Passivation of Perovskite Film for Efficient Solar Cells. *Nat. Photonics* **2019**, *13* (7), 460−466.

(8) Jena, A. K.; Kulkarni, A.; Miyasaka, T. Halide Perovskite Photovoltaics: Background, Status, and Future Prospects. *Chem. Rev.* **2019**, *119* (5), 3036−3103.

(9) NREL Best Research-cell Efficiencies Chart; https://www.nrel.gov/pv/cell-efficiency.html.

(10) Stranks, S. D.; Eperon, G. E.; Grancini, G.; Menelaou, C.; Alcocer, M. J. P.; Leijtens, T.; Herz, L. M.; Petrozza, A.; Snaith, H. J. Electron-Hole Diffusion Lengths Exceeding 1 Micrometer in an Organometal Trihalide Perovskite Absorber. *Science* **2013**, *342* (6156), 341−344.

(11) Tong, J.; Song, Z.; Kim, D. H.; Chen, X.; Chen, C.; Palmstrom, A. F.; Ndione, P. F.; Reese, M. O.; Dunfield, S. P.; Reid, O. G.; Liu, J.; Zhang, F.; Harvey, S. P.; Li, Z.; Christensen, S. T.; Teeter, G.; Zhao, D.; Al-Jassim, M. M.; van Hest, M. F. A. M.; Beard, M. C.; Shaheen, S. E.; Berry, J. J.; Yan, Y.; Zhu, K. Carrier Lifetimes of > 1 μs in Sn-Pb Perovskites Enable Efficient All-Perovskite Tandem Solar Cells. *Science* **2019**, *364* (6439), 475−479.

(12) Dong, Q.; Fang, Y.; Shao, Y.; Mulligan, P.; Qiu, J.; Cao, L.; Huang, J. Electron-Hole Diffusion Lengths > 175 μm in Solution-Grown $CH_3NH_3PbI_3$ Single Crystals. *Science* **2015**, *347* (6225), 967−970.

(13) Eames, C.; Frost, J. M.; Barnes, P. R. F.; O'Regan, B. C.; Walsh, A.; Islam, M. S. Ionic Transport in Hybrid Lead Iodide Perovskite Solar Cells. *Nat. Commun.* **2015**, *6* (1), 7497.

(14) Wang, R.; Mujahid, M.; Duan, Y.; Wang, Z.-K.; Xue, J.; Yang, Y. A Review of Perovskites Solar Cell Stability. *Adv. Funct. Mater.* **2019**, *29* (47), 1808843.
(15) Wang, Q.; Phung, N.; Di Girolamo, D.; Vivo, P.; Abate, A. Enhancement in Lifespan of Halide Perovskite Solar Cells. *Energy Environ. Sci.* **2019**, *12* (3), 865−886.
(16) Zhang, F.; Yang, X.; Cheng, M.; Wang, W.; Sun, L. Boosting the Efficiency and the Stability of Low Cost Perovskite Solar Cells by Using Cupc Nanorods as Hole Transport Material and Carbon as Counter Electrode. *Nano Energy* **2016**, *20*, 108−116.
(17) Park, N.-G.; Grätzel, M.; Miyasaka, T.; Zhu, K.; Emery, K. Towards Stable and Commercially Available Perovskite Solar Cells. *Nat. Energy* **2016**, *1* (11), 16152.
(18) Lai, H.; Kan, B.; Liu, T.; Zheng, N.; Xie, Z.; Zhou, T.; Wan, X.; Zhang, X.; Liu, Y.; Chen, Y. Two-Dimensional Ruddlesden−Popper Perovskite with Nanorod-Like Morphology for Solar Cells with Efficiency Exceeding 15%. *J. Am. Chem. Soc.* **2018**, *140* (37), 11639−11646.
(19) Roose, B.; Wang, Q.; Abate, A. The Role of Charge Selective Contacts in Perovskite Solar Cell Stability. *Adv. Energy Mater.* **2018**, *9* (5), 1803140.
(20) Han, T.-H.; Tan, S.; Xue, J.; Meng, L.; Lee, J.-W.; Yang, Y. Interface and Defect Engineering for Metal Halide Perovskite Optoelectronic Devices. *Adv. Mater.* **2019**, *31* (47), 1803515.
(21) Grancini, G.; Nazeeruddin, M. K. Dimensional Tailoring of Hybrid Perovskites for Photovoltaics. *Nature Reviews Materials* **2019**, *4* (1), 4−22.
(22) Uddin, A.; Upama, M. B.; Yi, H.; Duan, L. Encapsulation of Organic and Perovskite Solar Cells: A Review. *Coatings* **2019**, *9* (2), 65.
(23) Cheng, M.; Chen, C.; Yang, X.; Huang, J.; Zhang, F.; Xu, B.; Sun, L. Novel Small Molecular Materials Based on Phenoxazine Core Unit for Efficient Bulk Heterojunction Organic Solar Cells and Perovskite Solar Cells. *Chem. Mater.* **2015**, *27* (5), 1808−1814.
(24) Chen, H.; Bryant, D.; Troughton, J.; Kirkus, M.; Neophytou, M.; Miao, X.; Durrant, J. R.; McCulloch, I. One-Step Facile Synthesis of a Simple Hole Transport Material for Efficient Perovskite Solar Cells. *Chem. Mater.* **2016**, *28* (8), 2515−2518.
(25) Saliba, M.; Orlandi, S.; Matsui, T.; Aghazada, S.; Cavazzini, M.; Correa-Baena, J.-P.; Gao, P.; Scopelliti, R.; Mosconi, E.; Dahmen, K.-H.; De Angelis, F.; Abate, A.; Hagfeldt, A.; Pozzi, G.; Graetzel, M.; Nazeeruddin, M. K. A Molecularly Engineered Hole-Transporting Material for Efficient Perovskite Solar Cells. *Nat. Energy* **2016**, *1* (2), 15017.
(26) Xu, B.; Zhang, J.; Hua, Y.; Liu, P.; Wang, L.; Ruan, C.; Li, Y.; Boschloo, G.; Johansson, E. M. J.; Kloo, L.; Hagfeldt, A.; Jen, A. K. Y.; Sun, L. Tailor-Making Low-Cost Spiro[fluorene-9,9′-xanthene]-Based 3D Oligomers for Perovskite Solar Cells. *Chem.* **2017**, *2* (5), 676−687.
(27) Ge, Q.-Q.; Shao, J.-Y.; Ding, J.; Deng, L.-Y.; Zhou, W.-K.; Chen, Y.-X.; Ma, J.-Y.; Wan, L.-J.; Yao, J.; Hu, J.-S.; Zhong, Y.-W. A Two-Dimensional Hole-Transporting Material for High-Performance Perovskite Solar Cells with 20% Average Efficiency. *Angew. Chem., Int. Ed.* **2018**, *57* (34), 10959−10965.
(28) Chiykowski, V. A.; Cao, Y.; Tan, H.; Tabor, D. P.; Sargent, E. H.; Aspuru-Guzik, A.; Berlinguette, C. P. Precise Control of Thermal and Redox Properties of Organic Hole-Transport Materials. *Angew. Chem., Int. Ed.* **2018**, *57* (47), 15529−15533.
(29) Christians, J. A.; Schulz, P.; Tinkham, J. S.; Schloemer, T. H.; Harvey, S. P.; Tremolet de Villers, B. J.; Sellinger, A.; Berry, J. J.; Luther, J. M. Tailored Interfaces of Unencapsulated Perovskite Solar Cells for > 1,000 h Operational Stability. *Nat. Energy* **2018**, *3* (1), 68−74.
(30) Vaitukaityte, D.; Wang, Z.; Malinauskas, T.; Magomedov, A.; Bubniene, G.; Jankauskas, V.; Getautis, V.; Snaith, H. J. Efficient and Stable Perovskite Solar Cells Using Low-Cost Aniline-Based Enamine Hole-Transporting Materials. *Adv. Mater.* **2018**, *30* (45), 1803735.
(31) Shen, C.; Wu, Y.; Zhang, H.; Li, E.; Zhang, W.; Xu, X.; Wu, W.; Tian, H.; Zhu, W.-H. Semi-Locked Tetrathienylethene as a Building Block for Hole-Transporting Materials: Toward Efficient and Stable Perovskite Solar Cells. *Angew. Chem., Int. Ed.* **2019**, *58* (12), 3784−3789.
(32) Salbeck, J.; Yu, N.; Bauer, J.; Weissörtel, F.; Bestgen, H. Low Molecular Organic Glasses for Blue Electroluminescence. *Synth. Met.* **1997**, *91* (1), 209−215.
(33) Bach, U.; Lupo, D.; Comte, P.; Moser, J. E.; Weissörtel, F.; Salbeck, J.; Spreitzer, H.; Grätzel, M. Solid-State Dye-Sensitized Mesoporous TiO_2 Solar Cells with High Photon-to-Electron Conversion Efficiencies. *Nature* **1998**, *395* (6702), 583−585.
(34) Kim, M.; Kim, G.-H.; Lee, T. K.; Choi, I. W.; Choi, H. W.; Jo, Y.; Yoon, Y. J.; Kim, J. W.; Lee, J.; Huh, D.; Lee, H.; Kwak, S. K.; Kim, J. Y.; Kim, D. S. Methylammonium Chloride Induces Intermediate Phase Stabilization for Efficient Perovskite Solar Cells. *Joule* **2019**, *3* (9), 2179−2192.
(35) Noh, J. H.; Jeon, N. J.; Choi, Y. C.; Nazeeruddin, M. K.; Grätzel, M.; Seok, S. I. Nanostructured $TiO_2/CH_3NH_3PBbI_3$ Heterojunction Solar Cells Employing Spiro-OMeTAD/Co-Complex as Hole-Transporting Material. *J. Mater. Chem. A* **2013**, *1* (38), 11842−11847.
(36) Abate, A.; Leijtens, T.; Pathak, S.; Teuscher, J.; Avolio, R.; Errico, M. E.; Kirkpatrik, J.; Ball, J. M.; Docampo, P.; McPherson, I.; Snaith, H. J. Lithium Salts as "Redox Active" p-Type Dopants for Organic Semiconductors and Their Impact in Solid-State Dye-Sensitized Solar Cells. *Phys. Chem. Chem. Phys.* **2013**, *15* (7), 2572−2579.
(37) Burschka, J.; Dualeh, A.; Kessler, F.; Baranoff, E.; Cevey-Ha, N.-L.; Yi, C.; Nazeeruddin, M. K.; Grätzel, M. Tris(2-(1H-pyrazol-1-yl)pyridine)cobalt(III) as p-Type Dopant for Organic Semiconductors and Its Application in Highly Efficient Solid-State Dye-Sensitized Solar Cells. *J. Am. Chem. Soc.* **2011**, *133* (45), 18042−18045.
(38) Leijtens, T.; Lim, J.; Teuscher, J.; Park, T.; Snaith, H. J. Charge Density Dependent Mobility of Organic Hole-Transporters and Mesoporous TiO_2 Determined by Transient Mobility Spectroscopy: Implications to Dye-Sensitized and Organic Solar Cells. *Adv. Mater.* **2013**, *25* (23), 3227−3233.
(39) Fabregat-Santiago, F.; Bisquert, J.; Cevey, L.; Chen, P.; Wang, M.; Zakeeruddin, S. M.; Grätzel, M. Electron Transport and Recombination in Solid-State Dye Solar Cell with Spiro-OMeTAD as Hole Conductor. *J. Am. Chem. Soc.* **2009**, *131* (2), 558−562.
(40) Liu, J.; Wu, Y.; Qin, C.; Yang, X.; Yasuda, T.; Islam, A.; Zhang, K.; Peng, W.; Chen, W.; Han, L. A Dopant-Free Hole-Transporting Material for Efficient and Stable Perovskite Solar Cells. *Energy Environ. Sci.* **2014**, *7* (9), 2963−2967.
(41) Jena, A. K.; Ikegami, M.; Miyasaka, T. Severe Morphological Deformation of Spiro-OMeTAD in $(CH_3NH_3)PbI_3$ Solar Cells at High Temperature. *ACS Energy Lett.* **2017**, *2* (8), 1760−1761.
(42) Parthasarathy, G.; Shen, C.; Kahn, A.; Forrest, S. R. Lithium Doping of Semiconducting Organic Charge Transport Materials. *J. Appl. Phys.* **2001**, *89* (9), 4986−4992.
(43) Juarez-Perez, E. J.; Leyden, M. R.; Wang, S.; Ono, L. K.; Hawash, Z.; Qi, Y. Role of the Dopants on the Morphological and Transport Properties of Spiro-MeOTAD Hole Transport Layer. *Chem. Mater.* **2016**, *28* (16), 5702−5709.
(44) Rakstys, K.; Paek, S.; Gao, P.; Gratia, P.; Marszalek, T.; Grancini, G.; Cho, K. T.; Genevicius, K.; Jankauskas, V.; Pisula, W.; Nazeeruddin, M. K. Molecular Engineering of Face-On Oriented Dopant-Free Hole Transporting Material for Perovskite Solar Cells with 19% PCE. *J. Mater. Chem. A* **2017**, *5* (17), 7811−7815.
(45) Xu, B.; Bi, D.; Hua, Y.; Liu, P.; Cheng, M.; Grätzel, M.; Kloo, L.; Hagfeldt, A.; Sun, L. A Low-Cost Spiro[fluorene-9,9'-xanthene]-Based Hole Transport Material for Highly Efficient Solid-State Dye-Sensitized Solar Cells and Perovskite Solar Cells. *Energy Environ. Sci.* **2016**, *9* (3), 873−877.
(46) Zhou, W.; Wen, Z.; Gao, P. Less is More: Dopant-Free Hole Transporting Materials for High-Efficiency Perovskite Solar Cells. *Adv. Energy Mater.* **2018**, *8* (9), 1702512.
(47) Hou, W.; Xiao, Y.; Han, G.; Lin, J.-Y. The Applications of Polymers in Solar Cells: A Review. *Polymers* **2019**, *11* (1), 143.

https://dx.doi.org/10.1021/jacs.0c08352
J. Am. Chem. Soc. 2020, 142, 17681−17692

(48) Al-Hussein, M.; Herzig, E. M.; Schindler, M.; Löhrer, F.; Palumbiny, C. M.; Wang, W.; Roth, S. V.; Müller-Buschbaum, P. Comparative Study of the Nanomorphology of Spray and Spin Coated PTB7 Polymer: Fullerene Films. *Polym. Eng. Sci.* **2016**, *56* (8), 889−894.
(49) Su, B.; Caller-Guzman, H. A.; Körstgens, V.; Rui, Y.; Yao, Y.; Saxena, N.; Santoro, G.; Roth, S. V.; Müller-Buschbaum, P. Macroscale and Nanoscale Morphology Evolution during in Situ Spray Coating of Titania Films for Perovskite Solar Cells. *ACS Appl. Mater. Interfaces* **2017**, *9* (50), 43724−43732.
(50) Kim, G.-W.; Kang, G.; Kim, J.; Lee, G.-Y.; Kim, H. I.; Pyeon, L.; Lee, J.; Park, T. Dopant-Free Polymeric Hole Transport Materials for Highly Efficient and Stable Perovskite Solar Cells. *Energy Environ. Sci.* **2016**, *9* (7), 2326−2333.
(51) Liao, H.-C.; Tam, T. L. D.; Guo, P.; Wu, Y.; Manley, E. F.; Huang, W.; Zhou, N.; Soe, C. M. M.; Wang, B.; Wasielewski, M. R.; Chen, L. X.; Kanatzidis, M. G.; Facchetti, A.; Chang, R. P. H.; Marks, T. J. Dopant-Free Hole Transporting Polymers for High Efficiency, Environmentally Stable Perovskite Solar Cells. *Adv. Energy Mater.* **2016**, *6* (16), 1600502.
(52) Lee, J.; Malekshahi Byranvand, M.; Kang, G.; Son, S. Y.; Song, S.; Kim, G.-W.; Park, T. Green-Solvent-Processable, Dopant-Free Hole-Transporting Materials for Robust and Efficient Perovskite Solar Cells. *J. Am. Chem. Soc.* **2017**, *139* (35), 12175−12181.
(53) Zhang, L.; Liu, C.; Zhang, J.; Li, X.; Cheng, C.; Tian, Y.; Jen, A. K.-Y.; Xu, B. Intensive Exposure of Functional Rings of a Polymeric Hole-Transporting Material Enables Efficient Perovskite Solar Cells. *Adv. Mater.* **2018**, *30* (39), 1804028.
(54) Cai, B.; Xing, Y.; Yang, Z.; Zhang, W.-H.; Qiu, J. High Performance Hybrid Solar Cells Sensitized by Organolead Halide Perovskites. *Energy Environ. Sci.* **2013**, *6* (5), 1480−1485.
(55) Cai, F.; Cai, J.; Yang, L.; Li, W.; Gurney, R. S.; Yi, H.; Iraqi, A.; Liu, D.; Wang, T. Molecular Engineering of Conjugated Polymers for Efficient Hole Transport and Defect Passivation in Perovskite Solar Cells. *Nano Energy* **2018**, *45*, 28−36.
(56) Kim, G.-W.; Lee, J.; Kang, G.; Kim, T.; Park, T. Donor−Acceptor Type Dopant-Free, Polymeric Hole Transport Material for Planar Perovskite Solar Cells (19.8%). *Adv. Energy Mater.* **2018**, *8* (4), 1701935.
(57) Kranthiraja, K.; Gunasekar, K.; Kim, H.; Cho, A.-N.; Park, N.-G.; Kim, S.; Kim, B. J.; Nishikubo, R.; Saeki, A.; Song, M.; Jin, S.-H. High-Performance Long-Term-Stable Dopant-Free Perovskite Solar Cells and Additive-Free Organic Solar Cells by Employing Newly Designed Multirole π-Conjugated Polymers. *Adv. Mater.* **2017**, *29* (23), 1700183.
(58) Liao, S.-H.; Jhuo, H.-J.; Cheng, Y.-S.; Chen, S.-A. Fullerene Derivative-Doped Zinc Oxide Nanofilm as the Cathode of Inverted Polymer Solar Cells with Low-Bandgap Polymer (PTB7-Th) for High Performance. *Adv. Mater.* **2013**, *25* (34), 4766−4771.
(59) Meng, L.; Zhang, Y.; Wan, X.; Li, C.; Zhang, X.; Wang, Y.; Ke, X.; Xiao, Z.; Ding, L.; Xia, R.; Yip, H.-L.; Cao, Y.; Chen, Y. Organic and Solution-Processed Tandem Solar Cells with 17.3% Efficiency. *Science* **2018**, *361* (6407), 1094−1098.
(60) Zhang, F.; Yao, Z.; Guo, Y.; Li, Y.; Bergstrand, J.; Brett, C. J.; Cai, B.; Hajian, A.; Guo, Y.; Yang, X.; Gardner, J. M.; Widengren, J.; Roth, S. V.; Kloo, L.; Sun, L. Polymeric, Cost-Effective, Dopant-Free Hole Transport Materials for Efficient and Stable Perovskite Solar Cells. *J. Am. Chem. Soc.* **2019**, *141* (50), 19700−19707.
(61) Würthner, F. Perylene Bisimide Dyes as Versatile Building Blocks for Functional Supramolecular Architectures. *Chem. Commun.* **2004**, *14*, 1564−1579.
(62) Li, C.; Liu, Z.; Schöneboom, J.; Eickemeyer, F.; Pschirer, N. G.; Erk, P.; Herrmann, A.; Müllen, K. Perylenes as Sensitizers in Hybrid Solar Cells: How Molecular Size Influences Performance. *J. Mater. Chem.* **2009**, *19* (30), 5405−5415.
(63) Yao, Z.; Zhang, M.; Wu, H.; Yang, L.; Li, R.; Wang, P. Donor/Acceptor Indenoperylene Dye for Highly Efficient Organic Dye-Sensitized Solar Cells. *J. Am. Chem. Soc.* **2015**, *137* (11), 3799−3802.
(64) Yao, Z.; Wu, H.; Li, Y.; Wang, J.; Zhang, J.; Zhang, M.; Guo, Y.; Wang, P. Dithienopicenocarbazole as the Kernel Module of Low-Energy-Gap Organic Dyes for Efficient Conversion of Sunlight to Electricity. *Energy Environ. Sci.* **2015**, *8* (11), 3192−3197.
(65) Spano, F. C. The Spectral Signatures of Frenkel Polarons in H- and J-Aggregates. *Acc. Chem. Res.* **2010**, *43* (3), 429−439.
(66) Müller-Buschbaum, P. The Active Layer Morphology of Organic Solar Cells Probed with Grazing Incidence Scattering Techniques. *Adv. Mater.* **2014**, *26* (46), 7692−7709.
(67) Wang, R.; Tong, Y.; Wang, K.; Xia, S.; Kentzinger, E.; Soltwedel, O.; Müller-Buschbaum, P.; Frielinghaus, H. Monitoring the Morphological Evolution in Mixed-Dimensional Lead Bromide Perovskite Films with Lamellar-Stacked Perovskite Nanoplatelets. *Nanoscale Horiz* **2019**, *4* (5), 1139−1144.
(68) Guo, X.; Zhou, N.; Lou, S. J.; Smith, J.; Tice, D. B.; Hennek, J. W.; Ortiz, R. P.; Navarrete, J. T. L.; Li, S.; Strzalka, J.; Chen, L. X.; Chang, R. P. H.; Facchetti, A.; Marks, T. J. Polymer Solar Cells with Enhanced Fill Factors. *Nat. Photonics* **2013**, *7* (10), 825−833.
(69) Zhang, Q.; Kelly, M. A.; Bauer, N.; You, W. The Curious Case of Fluorination of Conjugated Polymers for Solar Cells. *Acc. Chem. Res.* **2017**, *50* (9), 2401−2409.
(70) Fang, L.; Zheng, A.; Ren, M.; Xie, X.; Wang, P. Unraveling the Structure−Property Relationship of Molecular Hole-Transporting Materials for Perovskite Solar Cells. *ACS Appl. Mater. Interfaces* **2019**, *11* (42), 39001−39009.
(71) Slater, J. C. Atomic Radii in Crystals. *J. Chem. Phys.* **1964**, *41* (10), 3199−3204.
(72) Clementi, E.; Raimondi, D. L.; Reinhardt, W. P. Atomic Screening Constants from SCF Functions. II. Atoms with 37 to 86 Electrons. *J. Chem. Phys.* **1967**, *47* (4), 1300−1307.
(73) Moulder, J. F. *Handbook of X-ray Photoelectron Spectroscopy: A Reference Book of Standard Spectra for Identification and Interpretation of XPS Data*; Physical Electronics, 1995; pp 230−232.
(74) Zhang, F.; Cong, J.; Li, Y.; Bergstrand, J.; Liu, H.; Cai, B.; Hajian, A.; Yao, Z.; Wang, L.; Hao, Y.; Yang, X.; Gardner, J. M.; Ågren, H.; Widengren, J.; Kloo, L.; Sun, L. A Facile Route to Grain Morphology Controllable Perovskite Thin Films towards Highly Efficient Perovskite Solar Cells. *Nano Energy* **2018**, *53*, 405−414.
(75) Gonzalez-Pedro, V.; Juarez-Perez, E. J.; Arsyad, W.-S.; Barea, E. M.; Fabregat-Santiago, F.; Mora-Sero, I.; Bisquert, J. General Working Principles of $CH_3NH_3PbX_3$ Perovskite Solar Cells. *Nano Lett.* **2014**, *14* (2), 888−893.

https://dx.doi.org/10.1021/jacs.0c08352
J. Am. Chem. Soc. 2020, 142, 17681−17692